Enzalutamide, an Androgen Receptor Antagonist, Enhances Myeloid Cell–Mediated Immune Suppression and Tumor Progression

Camila R. Consiglio[1], Olga Udartseva[2], Kimberly D. Ramsey[2], Chioma Bush[2], and Sandra O. Gollnick[1,2]

ABSTRACT

Androgen receptor (AR) antagonism increases overall survival in prostate cancer; however, treatment failure leads to tumor progression and patient mortality. The effect of AR modulation on AR^+ nontumor cells that participate in the resistance to AR antagonism is poorly understood. Tumor-infiltrating myeloid cells, including macrophages and myeloid-derived suppressor cells (MDSC), express AR and promote prostate cancer progression. We investigated how AR antagonism affects myeloid cell function and metabolism in an AR-independent murine colon tumor model. Systemic blockade of AR with enzalutamide resulted in increased MC-38 tumor growth *in vivo* even when AR was knocked out of MC-38 tumor cells. MC-38 tumor growth was also increased when immunocompetent, but not immunodeficient, mice were coinjected with tumor cells and MDSCs treated with enzalutamide or lacking AR, suggesting that AR regulated the ability of MDSCs to suppress adaptive immunity. Myeloid AR-knockout male mice also displayed increased growth of TRAMP C2 prostate tumors when compared with wild type. Inhibition of AR signaling suppressed mitochondrial respiration in myeloid cells via MPC/AMPK signaling pathways; suppression of mitochondrial respiration increased MDSC tumor–promoting functions. Our work showed that AR regulates a tumor-promoting myeloid cell phenotype and influences myeloid cell metabolism. These findings suggest that tumor resistance to AR antagonism is due, in part, to changes in myeloid cell function and metabolism.

Introduction

Prostate cancer has the highest malignancy rates and is the second leading cause of cancer-related mortality in men. Hormone ablation therapy is a commonly used treatment for patients with prostate cancer, as early-stage prostate tumors require androgens for growth. Limiting the amount and function of androgen decreases tumor cell proliferation, reduces tumor sizes, and improves overall survival (1, 2). Androgen deprivation therapy (ADT) reduces testosterone concentrations in the blood, whereas antiandrogen therapy directly inhibits androgen receptor (AR) signaling in prostate cells. Although, initially effective, hormone therapy eventually fails in a proportion of patients and leads to progression of castration-resistant prostate cancer (CRPC; ref. 1). Various tumor cell intrinsic mechanisms are described for treatment resistance, such as genetic alterations of AR (amplifications, mutations, and splice variants) and the upregulation of pathways that support AR signaling (1).

Systemic hormone therapy might also affect the tumor microenvironment through modulation of AR^+ cells in the tumor niche (3–6). Myeloid cells in the tumor niche, including tumor-associated macrophages (TAM) and myeloid-derived suppressor cells (MDSC), promote tumor development and progression by inducing inflammation, immunosuppression, and angiogenesis, thus supporting treatment resistance (4, 7, 8). Myeloid cell infiltration is associated with poor cancer prognosis (9, 10). The role of AR expression by myeloid cells is controversial in murine prostate tumor models. Genetic deletion of AR in macrophages delays initial tumorigenesis (4) but increases progression and metastasis (11). ADT and AR antagonism with the antiandrogen, enzalutamide, increases TAM infiltration in murine prostate tumors, leading to prostate cancer progression (12). Thus, the direct role of AR in myeloid cell function in cancer and their response to antiandrogen therapy remains unclear.

Myeloid cell function is highly dependent on metabolism (13) and upregulation of glycolysis increases tumor-promoting capacity of TAMs and immunosuppression by MDSCs (14–17). Androgen stimulation of AR in prostate cancer cells induces glycolysis (18). It is unknown whether AR antagonism modulates myeloid cell metabolism, and whether treatment-induced metabolic changes impact myeloid cell function.

To understand AR regulation of myeloid cells in tumors, we utilized the AR-independent MC-38 colon tumor model (19) and the TRAMP C2 prostate tumor model (20). The effect of AR on myeloid cell function was investigated using pharmacologic inhibition and myeloid cell–specific genetic deletion of AR. Pharmacologic blockade of AR in myeloid cells with enzalutamide increased their tumor-promoting capacity by inhibition of adaptive immunity. AR pharmacologic inhibition also induced VEGF and Arg1 expression, and directly increased the suppressive activity of MDSCs. Blocking AR signaling with enzalutamide altered myeloid cell metabolism by decreasing mitochondrial respiration and increasing glycolysis. The effects on metabolism were mediated in an MPC/AMPK-dependent manner. Our work suggests that resistance to AR antagonism and subsequent

[1]Department of Immunology, Roswell Park Comprehensive Cancer Center, Buffalo, New York. [2]Department of Cell Stress Biology, Roswell Park Comprehensive Cancer Center, Buffalo, New York.

Note: Supplementary data for this article are available at Cancer Immunology Research Online (http://cancerimmunolres.aacrjournals.org/).

Current address for C.R. Consiglio: Science for Life Laboratory, Department of Women's and Children's Health, Karolinska Institutet, Solna, Sweden; and current address for C. Bush, Boonshoft School of Medicine, Wright State University, Dayton, Ohio.

Corresponding Author: Sandra O. Gollnick, Roswell Park Cancer Institute, Elm & Carlton Streets, Buffalo, NY 14263. Phone: 716-845-8877; Fax: 716-845-4920; E-mail: sandra.gollnick@roswellpark.org

Cancer Immunol Res 2020;8:1215–27

doi: 10.1158/2326-6066.CIR-19-0371

relapse of CRPC was due, in part, to the effects of AR antagonism on myeloid cell function and metabolism.

Material and Methods

Animal studies

Seven- to 10-week-old C57BL/6J male and female and B6-SCID male mice were purchased from Taconic Laboratory and the LysM^{cre} C57BL/6 male mice were purchased from The Jackson Laboratory. Male SCID pathogen-free mice ages 7–8 weeks were obtained through the Laboratory Animal Resource of Roswell Park Comprehensive Cancer Center (RPCCC, Buffalo, NY). AR^{floxed} mice were generated by De Gendt Laboratory at Katholieke Universiteit Leuven (Leuven, Belgium; ref. 21) and kindly shared by the Agoulnik Laboratory at Florida International University (Miami, FL). GFP^{+} mice were kindly donated by Dr. Andrei Gudkov laboratory at Roswell Park Cancer Institute (Buffalo, NY). For the generation of myeloid AR-knockout (MARKO) mice, Lys-M^{cre} males were crossed with AR^{floxed} females to generate MARKO males. Mice were housed in microisolator cages in a laminar flow unit under ambient light at 24°C. The RPCCC Institutional Animal Care and Use Committee approved all procedures and experiments for this study.

Genotyping

Tail clips of littermates from Lys-M^{cre} and AR^{floxed} breeding pairs were digested in Tail Lysis Buffer (Viagen Biotech, 102-T) with 200 μg proteinase K (Viagen Biotech, 502-PK) following the manufacturer's instructions, and DNA concentrations were determined using a Photometer (Bio-Rad). For PCR reactions, Platinum Taq DNA Polymerase was used following the manufacturer's instructions for PCR Reaction (Thermo Fisher Scientific, 10966018), with AR PCR primers forward: 5′ AGCCTGTATACTCAGTTGGGG 3′ and reverse 5′ AATGCATCACATTAAGTTGATACC 3′. Wild-type (WT) AR band was genotyped as 855 bp, AR^{floxed} as 952 bp, and AR^{KO} as 404 bp.

Primary cultures

Bone marrow cells were isolated by flushing out bone marrow from femur and tibia with needle/syringe. Bone marrow–derived macrophages (BMDM) were generated by culturing 1×10^6 unfractioned bone marrow cells from C57BL/6 WT or MARKO male mice with 30 ng/mL M-CSF (Thermo Fisher Scientific, 14-8983-80) in 10 cm dishes or culturing 0.2×10^6 bone marrow cells in 6-well plates in phenol red-free RPMI1640 (Thermo Fisher Scientific, 11835030) supplemented with 100 μg/mL Penicillin-Streptomycin-Glutamine (Thermo Fisher Scientific, 10378016) and 10% FBS Premium Select (Atlanta, S11595) at 37°C and 5% CO_2 for 5 days. BMDMs generated in 10 cm dishes were used in flow cytometry, admixture, suppression, seahorse, and Western blot experiments, while BMDMs generated in 6-well plates were utilized in RNA experiments. Mature, day 5 BMDMs were then stimulated with DMSO or 5 μmol/L Enzalutamide (Selleckchem, S1250) and other pathway inhibitors (see below in this section) for 24 hours. Murine MDSCs were generated by culturing 2.5×10^6 unfractioned bone marrow cells from male WT, MARKO, or GFP^{+} C57BL/6 mice with 40 ng/mL GM-CSF (R&D Systems, 415-ML) and 40 ng/mL IL6 (PeproTech, 216-16) in the presence or absence of 5 μmol/L Enzalutamide (Selleckchem, S1250) and other pathway inhibitors (see below in this section) in 10 cm dishes in phenol red-free media RPMI1640 (Thermo Fisher Scientific, 11835030) supplemented with 100 μg/mL Penicillin-Streptomycin-Glutamine (Thermo Fisher Scientific, 10378016) and 10% FBS Premium Select (Atlanta, S11595) at 37°C and 5% CO_2 for 4 days (22). After 4 days of MDSC culture, MDSCs were harvested for use in assays. For intracellular cytokine detection, day 4 MDSCs were cultured with GolgiStop (BD Biosciences, 554724) following the manufacturer's instructions for 4 hours. The following inhibitors were utilized and diluted according to the manufacturer's instructions: mTOR (100 nmol/L Rapamycin, Selleckchem, S1039), HIF-1α (10 μmol/L YC-1, Selleckchem, S7958), AMPK (6.25 μmol/L Dorsomorphin, Selleckchem, S7306), AKT (5 μmol/L MK-2206, Selleckchem, S1076), MPC (40 μmol/L UK5509, Selleckchem, S5317), and 2-DG (1.5 mmol/L, Sigma, D6134).

Cell culture

Murine MC-38 colon cancer cells (purchased from Kerafast, ENH204 in 2018) were cultured in DMEM (Thermo Fisher Scientific, 11965-118) with 10% FBS Optima (Atlanta, S12495), 100 μg/mL Penicillin-Streptomycin-Glutamine (Thermo Fisher Scientific, 10378016), 0.1 mmol/L nonessential amino acids (Thermo Fisher Scientific, 11140035), 1 mmol/L sodium pyruvate (Thermo Fisher Scientific, 11360070), and 10 mmol/L HEPES (Thermo Fisher Scientific, 15630080) at 37°C and 5% CO_2. Human PC3M prostate tumor cells (obtained from Dr. I. Gelman, RPCCC, Buffalo, NY in 2016) were cultured in RPMI1640 (Thermo Fisher Scientific, 11875-119) with 10% FBS Optima (Atlanta, S12495) and 100 μg/mL Penicillin-Streptomycin-Glutamine (Thermo Fisher Scientific, 10378016) at 37°C and 5% CO_2. All cell lines were cultured for a maximum of 15 passages (maximum of 2 weeks). Cell lines were not authenticated in the past year and are routinely tested for *Mycoplasma*, only *Mycoplasma*-negative cells were used for experiments. For *in vitro* experiments, 0.066×10^6 MC-38 cells were plated in 6-well plates. On day 1, cells were treated with diluent DMSO or 5 μmol/L enzalutamide for 24, 48, 72, and 96 hours for cell number and viability assessment by trypan blue staining (>90% viability was used). TRAMP C2 prostate tumor cells (obtained from ATCC, CRL-2731 in 2016) were cultured in the presence of 10^{-8} mol/L Dihydrotestosterone (Sigma, D-073) at 37°C and 10% CO_2 and as described previously (20). MC-38 ARKO cells were generated using CRISPR/Cas9 gene editing. MC-38 cells were transfected with AR-Crispr/Cas9 KO (sc-419181, Santa Cruz Biotechnology) and AR-HDR (sc-419181-HDR) plasmids, which contain sequences encoding GFP or a puromycin resistance gene, respectively, for selection of ARKO cells, according to the manufacturer's instruction. MC-38 control cells were transfected with the pGIPZ-GFP plasmid. For transfection, plasmids in equivalent ratios were diluted in plasmid transfection medium (sc-108062) and mixed with UltraCruz transfection reagent (sc-395739). Prior to transfection, MC-38 growth medium was replaced with fresh antibiotic-free medium, and the transfection complexes (5 μg of each plasmid and 50 μL of transfection reagent in 1.5 mL of transfection medium) were added dropwise to the fresh antibiotic-free growth medium (10 mL in 100 mm dish). The medium was replaced in 24 hours. MC-38 cells were harvested 72 hours posttransfection and sorted for GFP expression (BD FACSAria II, BD Biosciences) to enrich the target population of transfected cells. GFP-expressing cells were plated in growth medium, and cells where Cas9-induced DNA cleavage has occurred were selected with puromycin. The ARKO phenotype of MC-38 cells was confirmed by Western blotting using the AR antibody (06-680, MilliporeSigma; Supplementary Fig. S1A).

In vivo tumor experiments and tumor processing

C57BL/6 males were inoculated subcutaneously on the shoulder with 100 μL of 10^5 or 10^6 MC-38 cells. When tumors inoculated with 10^6 MC-38 cells reached 100 mm^3, mice were treated with saline or enzalutamide 20 mg/kg daily by oral gavage in less than 5 mL/kg of

body weight. For admixture experiments, either 2×10^5 BMDMs or MDSCs were mixed in a 2:1 ratio with MC-38 cells in PBS, and 100 μL were implanted subcutaneously on the shoulder of C57BL/6 males. C57BL/6 and MARKO male mice were inoculated subcutaneously on the shoulder with 100 μL of 10^6 TRAMP C2 prostate tumor cells in PBS. SCID males were inoculated subcutaneously on the shoulder with 100 μL of 10^6 PC3M cells in PBS. Tumors were measured with an external caliper and tumor volume was calculated by volume = length × (width^2) ×1/2. Tumor growth was measured until tumors reached endpoint of 2,000 mm^3. A human prostate cancer xenograft (PCaX) was also studied (sample obtained with written consent and in accordance with the U.S. Common Rule), in collaboration with Dr. Barbara A. Foster (RPCCC, Buffalo, NY). PCaX was derived from 1 Caucasian male diagnosed with prostate cancer at 55 years of age. Tumor staging was IV Gleason primary/V Gleason secondary, T1c, N0, and M1b for tumors from a PCaX. PCaX tumor cells were implanted in NSG males, and when tumors reached 200 mm^3, mice were left either untreated or were treated with enzalutamide (25 mg/kg 5 days a week by oral gavage) until tumors reached the endpoint of 1,000 mm^3. Tumors were digested for 1 hour with 5 mg Collagenase (Sigma, C6885) and 50 μg DNaseI (Sigma, D4527-200KU) using gentleMACS octo Dissociator with heaters using gentleMACS C Tubes (Miltenyi Biotec) and program 37-m-TDK-3

Suppression assay

Spleens were collected and splenocytes were harvested from C57BL/6 male mice by mashing spleens, centrifuging, and lysing RBCs with RBC lysis buffer. Pan T cells were isolated by negative selection following the manufacturer's instructions (Miltenyi Biotec, 130-095-130 and 130-042-401) and Pan T cell enrichment was confirmed by flow cytometry (>90% CD3$^+$ T cells). Pan T cells were stained with CTV following the manufacturer's instructions to allow monitoring of T-cell proliferation through dye dilution (Thermo Fisher Scientific, C34557). CTV-stained Pan T cells were stimulated with anti-CD3/CD28 beads according to the manufacturer's instructions (Thermo Fisher Scientific, 11452D) in a 1:1 ratio, and MDSCs generated (see above primary cultures) were cultured with T cells in a ratio of 1:1, 1:2, and 1:4 MDSC:T cell for 4 days in phenol red-free RPMI1640 (Thermo Fisher Scientific, 11835030) supplemented with 100 μg/mL Penicillin-Streptomycin-Glutamine (Thermo Fisher Scientific, 10378016) and 10% FBS Premium Select (Atlanta, S11595). Cells were then stained with surface antibodies and analyzed for T-cell proliferation by flow cytometry (details under "Flow cytometry and ImageStream" section).

Isolation of CD11b$^+$ myeloid cells

CD11b$^+$ tumor-infiltrating cells were isolated by positive selection using magnetic bead separation following the manufacturer's instructions from single-cell suspensions generated from digested tumors (Miltenyi Biotec, 130-049-601 and 130-042-401). The purity of the enriched CD11b$^+$ cells was analyzed by flow cytometry (as described in "Flow cytometry and ImageStream" section), with the percentage of CD11b$^+$ cells being >80% for each separation.

RNA expression

Total RNA extraction was performed using the TRizol method according to the manufacturer's instructions (Thermo Fisher Scientific, 15596018). RNA concentrations were determined using a Photometer (Bio-Rad). cDNA synthesis was done using iScript cDNA Synthesis Kit (Bio-Rad, 1708891) and qPCR using SsoAdvanced Universal SYBR Green Supermix (Bio-Rad, 1725275), both according to the manufacturer's instructions. RNA expression was normalized to GAPDH levels. PCR primers were purchased from Integrated DNA Technologies. Primer sequences: Arg1 F 5′ AAGAAAAGGCCGATTC ACCT 3′, R 5′ CATGATATCTAGTCCTGAAAGG 3′; GAPDH F 5′ GGCAAGTTCAACGGCACAGTCAAG 3′, R 5′ GCACATACTCA-GCACCAGCATC AC 3′; GLUT1 F 5′ TATCGTCAACACGGCCTT-CAC TGT 3′, R 5′ CACAAAGCCAAAGA TGGCCACGAT 3′; IL1β F 5′ AAGGAGAACCAAGCAACGACAAAA 3′, R 5′TGGGGAA CTC-TGCAGACTCAAACT 3′; IL6 F 5′ GACAAAGCCAGAGTCCTTCA-GAGAG 3′, R 5′ CTAGGTTTGCC GAGTAGATCTC 3′; IL10 F 5′GAGACTTGCTCTTGCACTACC 3′, R 5′ CTCTCTTTTCT GCA-AGGCTG 3′; iNOS F 5′ CATCTCCGCAAATGTAGAGG 3′, R 5′ CAAACCCAAGGT CTACGTTCA 3′, MPC-2 F 5′ CCGCTTTACA-ACCACCCGGCA 3′, R 5′ CAGCACACAC CAATCCCCATTTCA 3′; TGFβ F 5′ CGTCAGACATTCGGGAAGA 3′, R 5′ CGTATCAG TGGGGGTCAGCA 3′; and VEGF F 5′ GAGGATGTCCTCACTCG-GATG 3′. Gene expression was determined by $2^{-\Delta\Delta C_t}$.

Flow cytometry and ImageStream

For flow cytometry and ImageStream staining, single-cell suspensions (digested tumors, BMDMs, and MDSCs) were treated for 10 minutes with 2:1 diluted mouse IgG:PBS (Thermo Fisher Scientific, 10400C) to block Fc receptors expressed on myeloid cells, followed by incubation with antibodies against cell surface molecules for 15 minutes. If intracellular staining was performed, cells were washed twice with FACs buffer, and cells were fixed/permeabilized (Thermo Fisher Scientific, 00-5523-00) for a minimum of 30 minutes, following the manufacturer's instructions. Permeabilized cells were treated with 2:1 diluted mouse IgG:PBS for 15 minutes, followed by incubation with antibodies against intracellular molecules for 30 minutes. Flow cytometry analysis was done by Flow Cytometer (BD Fortessa, BD LSRII). ImageStream analyses were performed using ImageStreamX Mark II. For p65 nuclear translocation control, MDSCs were stimulated with 100 ng/mL LPS (Sigma, L4516) and 2 μmol/L Ionomycin (Sigma, I0634) for 30 minutes at 37°C and 5% CO_2, stained for surface markers, fixed with 4% formaldehyde, permeabilized, and stained for intracellular markers. Flow cytometry and ImageStream analyses were performed using FlowJo and IDEAS, respectively. Surface antibodies used for flow cytometry and ImageStream were CD45 (BD Biosciences, 550994), CD11b (BD Biosciences, 553311), F4/80 (Thermo Fisher Scientific, 25-4801-82), CD115 (Thermo Fisher Scientific, 12-1152-82), Gr-1 (BD Biosciences, 553127), Ly6-G (BioLegend, 127612), Ly6-C (BioLegend, 128033), CD4 (BD Biosciences, 550954), CD8 (BD Biosciences, 553033), CD3e (Thermo Fisher Scientific, MA5-17658), and PD-L1 (Thermo Fisher Scientific, 12-5982-82). Antibodies against intracellular proteins were p65 (Cell Signaling Technology, 8242) and IL23p90 (Thermo Fisher Scientific, 50-7023-82). DAPI (Thermo Fisher Scientific, D1306) and LD Aqua (Thermo Fisher Scientific, L34957) were utilized to assess viability.

Protein expression

Protein lysates were made using MT Lysis Buffer (Sigma, C3228) in the presence of Protease (Sigma, P8340) and Phosphatase Inhibitors (Santa Cruz Biotechnology, sc-45044 and sc-45045) according to the manufacturer's instructions. Protein concentrations were determined using Bradford Assays (Bio-Rad, 5000006) and 20–40 μg of protein were run on 10% bis-tris Gels (Thermo Fisher Scientific, NP0303BOX) and then transferred to Nitrocellulose Membranes (Thermo Fisher Scientific, LC2001). Blots were probed for antibodies specific for ACC (Cell Signaling Technology, 3676S), p-ACC (Cell Signaling Technology, 11818S), AMPK (Cell Signaling Technology, 2532S), p-AMPK (Cell Signaling Technology, 2535S), AR (Sigma, 06-680), HIF1α (Cell

Signaling Technology, 3716), and β-Actin (Sigma, A2228). Secondary incubations were performed with HRP-anti-mouse (Santa Cruz Biotechnology, SC-516102) and HRP-anti-rabbit (Enzo, ADI-SAB-300-J). Primary antibody incubations were done overnight at 4°C and secondary antibody incubations were done for 1 hour at room temperature. Horseradish peroxidase (HRP) was developed (Bio-Rad 170-5061) and recorded using a Bio-Rad Imager (Bio-Rad ChemiDoc XRS+) and quantified using ImageLab Software (Bio-Rad).

Metabolism

Glucose uptake was assessed by culturing BMDMs (section primary cultures) treated with DMSO or 5 μmol/L enzalutamide for 9 hours, incubating cells with 100 μmol/L of fluorescence glucose analogue 2-NBDG (Thermo Fisher Scientific, N13195) in serum-free media without glucose for 30 minutes at 37°C, and quantifying glucose uptake by flow cytometry. Mitochondria were detected by flow cytometry with MitoTracker (Thermo Fisher Scientific, M7512), mitochondrial superoxide with MitoSOX (Thermo Fisher Scientific, M36008), and cellular reactive oxygen species with CM-H2DCFDA (Thermo Fisher Scientific, C6827) following the manufacturer's instructions.

A total of 10^5 MDSCs were plated in Cell-Tak Coated Plates (Thermo Fisher Scientific, CB40241) and 5×10^4 BMDMs were plated in XF96 cell culture microplates. Glycolytic rates were measured using Seahorse XF Glycolysis Stress Test Kit (Agilent, 103020-100) and mitochondrial respiration was measured with Seahorse XF Cell Mito Stress Test Kit (Agilent, 103015-100) according to the manufacturer's instructions by Roswell Park's Immune Analysis Facility. The carbonyl cyanide-4 (trifluoromethoxy) phenylhydrazone (FCCP) concentration utilized was 2 μmol/L. Fatty acid oxidation (FAO) was performed using the XF Palmitate-BSA FAO Substrate (Agilent, 102720-100) according to the manufacturer's instructions. FAO was calculated by subtracting values for before and after 40 μmol/L etomoxir treatment. Normalization of results was performed for adherent cells using methylene blue. Metabolic analyses were run on a Seahorse Xfe 96 Extracellular Flux Analyzer.

Statistical analysis

Statistical analyses were performed using GraphPad Prism 8.0 software. When comparing two groups, statistical analyses were performed using two-tailed Mann–Whitney or paired tests. When comparing two groups or more groups, one-way or two-way ANOVA were performed. Multiple comparison correction was applied when necessary. Tumor growth rate was analyzed using mixed model analyses for random slope and intercept. For metabolic profile plots, ellipses were estimated with ggplot2 in R. Differences were considered significant when P values were ≤0.05.

Results

AR antagonism increased colon tumor growth

Tumor-infiltrating myeloid cells can promote tumor development and progression by a number of mechanisms (8). The MC-38 is a murine colon tumor model that is syngeneic to C57BL/6 and exhibits myeloid-biased leukocyte infiltration (**Fig. 1A**; Supplementary Fig. S2A; ref. 19). MC-38 infiltrating $CD11b^+$ myeloid cells, which include TAMs and MDSCs, suppress T-cell proliferation *ex vivo* (**Fig. 1B**; Supplementary Fig. S2B). To examine the tumor-independent effects of AR blockade, we first investigated whether tumor cell expression of AR affected tumor growth. MC-38 cells have low expression of AR (Supplementary Fig. S1A); to assess the impact of AR on tumor growth, we used CRISPR/Cas9 gene editing to eliminate AR expression in MC-38 tumor cells (MC-38 ARKO). MC-38 ARKO cells had significantly lower expression of AR when compared with MC-38 cells ($P < 0.01$; Supplementary Fig. S1A). To assess whether AR had an indirect effect on tumor growth, we examined the effect of AR antagonist, enzalutamide, treatment on tumor growth. MC-38 and MC-38 ARKO tumor–bearing mice were treated daily with enzalutamide or saline through oral gavage (**Fig. 1C**). Tumor growth was not significantly different in male C57BL/6 mice inoculated with MC-38 control or MC-38 ARKO tumor cells (**Fig. 1D**). Enzalutamide treatment had a modest but significant effect on accelerating both MC-38 control and MC-38 ARKO tumor growth over that of saline-treated MC-38 and MC-38 ARKO tumor growth, respectively (**Fig. 1D**). In contrast, enzalutamide treatment of MC-38 cells *in vitro* reduced cell numbers over time (Supplementary Fig. S1B); the effects of enzalutamide on MC-38 ARKO cell proliferation was delayed as compared with the effect on control cells, which is likely a result of the reduced AR expression (Supplementary Fig. S1A). In total, these results supported the hypothesis that AR antagonism enhanced the tumor-promoting properties of nontumor cells. Enzalutamide treatment reduced the percentage of total infiltrating leukocytes, with this difference being attributed to decreased macrophage infiltration in tumors (Supplementary Fig. S1C).

AR inhibition increased tumor-promoting capacity of myeloid cells

AR antagonism potentially affects a variety of AR^+ cell types that compose the tumor microenvironment (4, 23). Because the majority of tumor-infiltrating immune cells in MC-38 tumors were myeloid biased (**Fig. 1A**; Supplementary Fig. S1C) and myeloid cells accelerates *in vivo* MC-38 tumor growth (Supplementary Fig. S3A), we next assessed whether genetic deletion or pharmacologic blockade of AR in macrophages or MDSCs could further enhance colon tumor growth. BMDMs and MDSCs were generated *in vitro* from Lys-M^{cre} AR^{floxed} MARKO or WT (C57BL/6) bone marrow in the presence of vehicle (DMSO) or enzalutamide. Myeloid cell populations were then mixed with 10^5 MC-38 tumor cells in a 2:1 myeloid:tumor cell ratio. The mixture was injected subcutaneously into C57BL/6 males and tumor progression was followed (**Fig. 2A**). Enzalutamide treatment of either BMDMs or MDSCs led to enhanced MC-38 tumor growth when compared with DMSO-treated myeloid cells (**Fig. 2B** and **C**). Myeloid cells from the initial GFP^+ MDSC:MC-38 mixture remained in tumors, with about 10% of total tumor-infiltrating macrophages and 6% of $Ly6G^+$ cells belonging to initial GFP^+ myeloid cells. Nonetheless, the enzalutamide-treated macrophages appeared to be more labile than their DMSO control counterparts (Supplementary Fig. S3B). DMSO- and enzalutamide-treated MDSC admixed tumors did not display differences in percentage of leukocyte subpopulation infiltration (Supplementary Fig. S3C). Mixture of MC-38 cells with MARKO myeloid cells also led to increased MC-38 tumor growth when compared with WT myeloid cells (**Fig. 2D** and **E**), indicating that inhibition of AR in myeloid cells enhanced their tumor-supporting capacity. The observed effects were AR dependent, as enzalutamide treatment of MARKO myeloid cells did not further alter MC-38 tumor growth (Supplementary Fig. S3D and S3E).

AR antagonism enhanced MDSC immunosuppression

MDSCs can support tumor growth by suppressing antitumor immune responses (8). Both genetic deletion and pharmacologic inhibition of MDSCs AR led to increased immunosuppressive

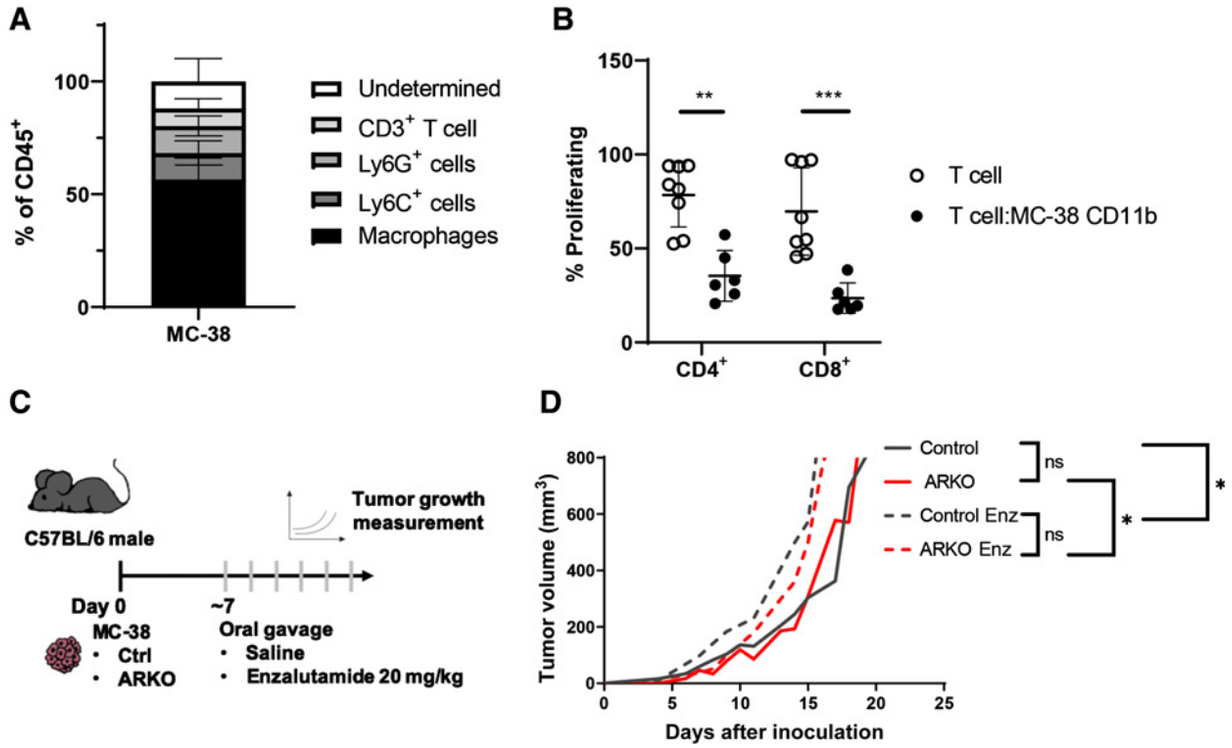

Figure 1.

AR inhibition accelerated MC-38 colon tumor growth. **A** and **B,** Eight- to 12-week-old C57BL/6 males were injected subcutaneously on the shoulder with 10^6 MC-38 colon tumor cells. Analyses were done when tumors reached 1,000 mm^3. Graphs show pooled data of two experiments with 3 mice per group per experiment and show mean and SD. **A,** Percentage of tumor-infiltrating leukocyte populations within $CD45^+$ cells determined by flow cytometry. $CD11b^+$ cells from tumors were isolated and measured for suppressive activity *in vitro*. **B,** Graph depicts proliferation of $CD4^+$ and $CD8^+$ T cells cocultured with tumor-infiltrating $CD11b^+$ cells (analyzed with Mann–Whitney test). **C,** C57BL/6 males were injected subcutaneously on the shoulder with 10^6 MC-38 control or MC-38 ARKO colon tumor cells and given saline or enzalutamide 20 mg/kg daily by oral gavage when tumors reached 100 mm^3. **D,** Tumor growth curve is depicted with pooled data of two experiments with 5 mice per group (analyzed with random mixed model). Mean tumor size versus time is shown. Black lines, MC-38 control; red lines, MC-38 ARKO; and dashed lines, enzalutamide treatment (*, $P < 0.05$; **, $P < 0.01$; ***, $P < 0.001$). Ctrl, control; Enz, enzalutamide; ns, not significant.

activity in suppression assays, as demonstrated by decreased $CD4^+$ and $CD8^+$ T-cell proliferation in MDSC cocultures (**Fig. 3A** and **B**). MDSCs treated with enzalutamide were not able to enhance MC-38 cancer growth in immunocompromised B6-SCID mice, indicating that enzalutamide enhanced MDSC tumor-supporting capacity through modulation of the adaptive immune system (**Fig. 3C**).

To further dissect how AR inhibition enhanced the tumor-supportive capacity of MDSCs, WT MDSCs were treated with enzalutamide and assessed for the expression of tumor-supporting factors. Enzalutamide-treated MDSCs had increased VEGF and Arg1 mRNA expression when compared with DMSO-treated MDSCs (**Fig. 3D**), suggesting that pharmacologic inhibition of AR might have enhanced tumor-supporting capability of MDSCs through promotion of angiogenesis (VEGF) and immunosuppression (Arg1). PD-L1 protein expression was increased upon enzalutamide treatment of MDSC (**Fig. 3E**; Supplementary Fig. S3F). MDSC IL23 secretion drives CRPC (7), although enzalutamide treatment did not affect IL23 protein expression in cultured MDSCs, suggesting an IL23-independent mechanism (**Fig. 3F**; Supplementary Fig. S3F). Genetic deletion of AR in MDSCs did not cause variation in VEGF or Arg1 mRNA expression (**Fig. 3D**), or in PD-L1 and IL23 protein expression (**Fig. 3E** and **F**).

AR antagonism increased myeloid cell glycolysis but decreased mitochondrial respiration

Myeloid cell function is influenced by their metabolic activity (13). To investigate whether AR blockade altered metabolism in myeloid cells, MDSCs were generated *in vitro* in the presence of enzalutamide and metabolic changes were assessed using Seahorse technology. Mitochondrial respiration parameters, such as basal respiration, ATP production from oxidative phosphorylation, and maximal respiration, were downregulated in MDSCs treated with enzalutamide when compared with DMSO-treated MDSCs (**Fig. 4A** and **B**). Enzalutamide treatment led to increased glycolytic rate and reduced glycolytic reserve in MDSCs when compared with DMSO-treated controls (**Fig. 4C** and **D**). Graphing of extracellular acidification rate (ECAR) versus oxygen consumption rate (OCR) showed increase in ECAR in MDSCs treated with enzalutamide (**Fig. 4E**). WT BMDMs treated *in vitro* with enzalutamide or BMDMs generated from bone marrow of MARKO mice also exhibited decreased mitochondrial respiration and increased glycolysis (**Fig. 4F**). The metabolic changes induced by enzalutamide were dependent on AR, as treatment of MARKO BMDMs with enzalutamide did not alter these metabolic changes (**Fig. 4F**). In addition, *in vitro* treatment of tumor-associated $CD11b^+$ cells from human prostate tumor xenografts models PC3M and PCaX led to a similar metabolic shift, indicating that tumor-associated myeloid cell metabolism was altered by AR inhibition (**Fig. 4G** and **H**).

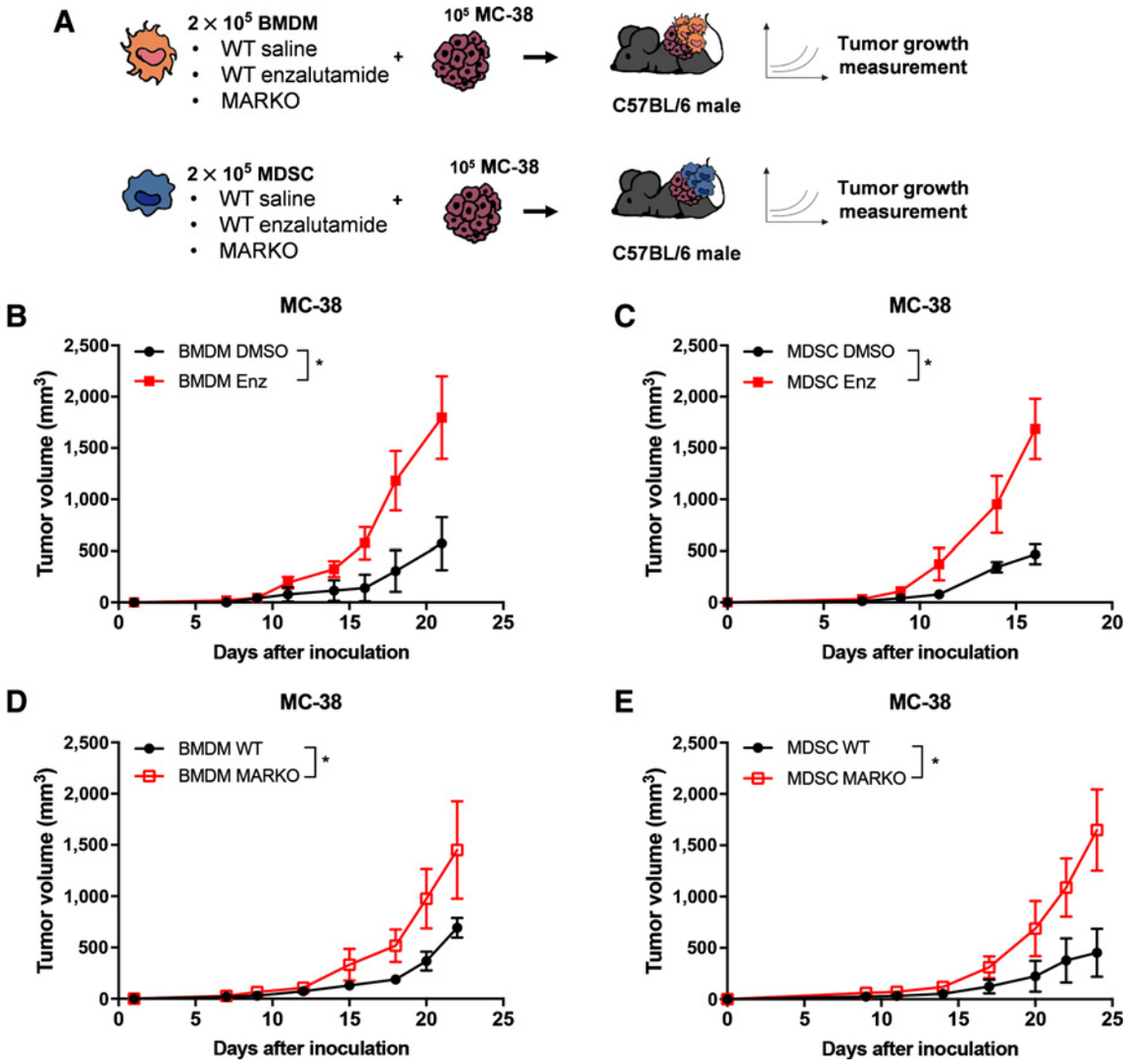

Figure 2.

Tumor-supporting properties of myeloid cells were increased upon AR inhibition. **A,** Experimental design: BMDMs and MDSCs were generated *in vitro* from WT or MARKO bone marrow of C57BL/6 males in the presence of DMSO or enzalutamide. BMDMs or MDSCs were then mixed with MC-38 tumor cells in a 2:1 myeloid:tumor cell ratio and implanted subcutaneously on the shoulder of C57BL/6 male mice. Graphs depict tumor growth curves of mice injected with MC-38 cells mixed with DMSO or enzalutamide-treated WT BMDMs (**B**) and MDSCs (**C**) or mixed with WT or MARKO BMDMs (**D**) or MDSCs (**E**). Graphs depict mean and SD of representative experiment of two to three experiments with 3 mice per group. For all graphs: black dots, DMSO-treated WT MDSCs; red solid squares, enzalutamide-treated MDSCs; and red empty squares, MARKO MDSCs. Statistical analyses were done using two-way ANOVA (*, $P < 0.05$). Enz, enzalutamide.

To determine whether systemic antiandrogen treatment of tumor-bearing animals affected tumor-associated myeloid cell metabolism, tumor-associated CD11b$^+$ cells were sorted from MC-38 tumor–bearing males treated *in vivo* with saline or enzalutamide and CD11b$^+$ cell metabolism was assessed. Similar to results observed *in vitro*, enzalutamide treatment led to decreased mitochondrial respiration and enhancement of glycolysis in tumor-associated CD11b$^+$ cells (**Fig. 4I**), suggesting that *in vivo* antiandrogen treatment altered the metabolism of tumor-associated myeloid cell directly.

AR antagonism–induced metabolic changes in myeloid cells are MPC-2/AMPK mediated

Increased glycolysis is frequently associated with a hypoxic environment, particularly in the tumor microenvironment, and linked to an increase in HIF1α (24). However, inhibition of HIF1α did not alter the effects of AR blockade on metabolism (Supplementary Fig. S4A). Myeloid cell polarization induces changes in metabolic pathway usage as a consequence of mTOR activation (25). The effect of AR blockade with enzalutamide on myeloid cellular metabolism was not affected by mTOR inhibition (Supplementary Fig. S4B). Increased AKT signaling is associated with increased glucose metabolism (26); inhibition of AKT did not affect enzalutamide-mediated changes in metabolism (Supplementary Fig. S4C). NF-κB signaling positively regulates myeloid cell tumor–promoting function (27), and is involved in regulation of glucose metabolism and resistance to enzalutamide in prostate cancer (28). AR pharmacologic inhibition in MDSCs did not alter NF-κB p65 levels or nuclear translocation (Supplementary Fig. S4D).

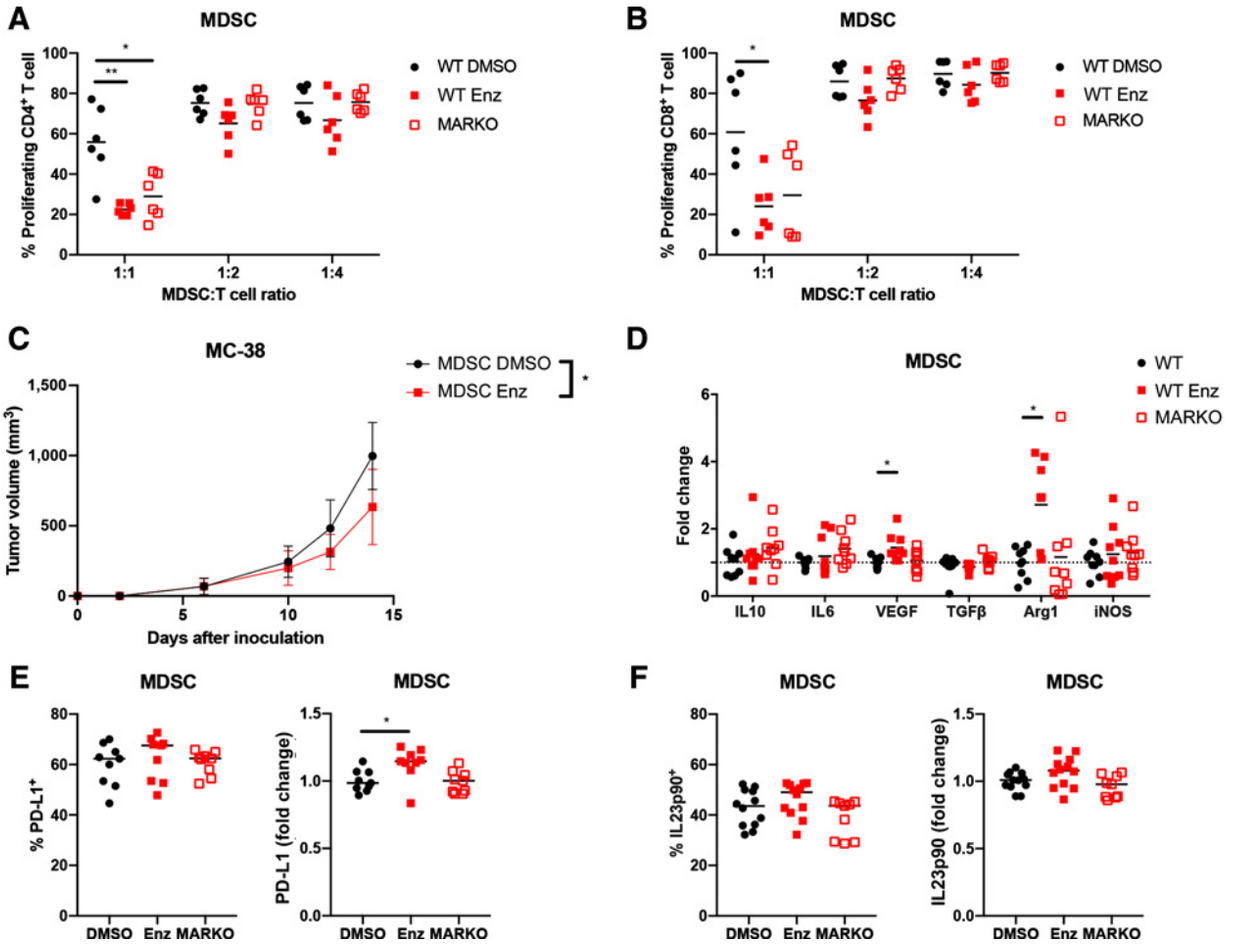

Figure 3.

AR inhibition enhanced MDSC immunosuppression. **A** and **B,** WT DMSO-treated, WT enzalutamide-treated, or MARKO MDSCs were cocultured with CTV-stained anti-CD3/CD28–stimulated CD3$^+$ T cells. Graphs depict results from two pooled experiments of three biological replicates each and indicate CD4$^+$ (**A**) and CD8$^+$ (**B**) T-cell proliferation, which indicates MDSC-suppressive potential assessed by flow cytometry. **C,** DMSO- and enzalutamide-treated MDSCs were generated, mixed in a 2:1 ratio with MC-38 tumor cells, and injected subcutaneously into B6-SCID males; plot indicates tumor growth (mean and SD) from two pooled experiments with 3 to 5 mice per group per experiment. **D,** RNA was extracted from WT DMSO-treated, WT enzalutamide-treated, or MARKO MDSCs, and gene expression was assessed by qRT-PCR. Graph depicts gene expression fold change relative to WT MDSCs. Dotted line indicates fold change of 1. MDSC protein expression was determined by flow cytometry for PD-L1 (**E**) and IL23p90 (**F**). For all graphs: black dots, WT MDSCs; red solid squares, WT enzalutamide MDSCs; and red empty squares, MARKO MDSCs. Kruskal–Wallis tests were first performed for **A**, **B**, and **D**. Lines indicate mean, and, where noted, error bars indicate SD. Significant comparisons were then compared by paired or Mann–Whitney tests with corrections. Two-way ANOVA was performed for data shown in **C** (*, $P < 0.05$; **, $P < 0.01$). Enz, enzalutamide.

AMPK regulates energy production through induction of glycolysis and FAO, and is implicated in myeloid cell function (29, 30). AR pharmacologic inhibition enhanced AMPK activation in MDSCs (**Fig. 5A**); AR pharmacologic inhibition and genetic deletion of AR upregulated AMPK expression in BMDMs (**Fig. 5B** and **C**). To investigate whether the metabolic changes associated with enzalutamide were due to AMPK induction in myeloid cells, BMDMs were treated with enzalutamide in the presence or absence of an AMPK inhibitor (dorsomorphin) for 24 hours. As observed previously (**Fig. 4**), enzalutamide treatment of myeloid cells decreased basal mitochondrial respiration, while increasing glycolytic rate. Enzalutamide was unable to downregulate basal mitochondrial respiration or upregulate glycolysis in the presence of AMPK inhibition in macrophages (**Fig. 5D** and **E**), indicating that enzalutamide-driven metabolic changes in macrophages were dependent on AMPK. AMPK inhibition of enzalutamide-treated MDSCs reversed the downregulation of basal mitochondrial respiration, but not the glycolytic upregulation induced by enzalutamide (**Fig. 5F** and **G**), suggesting that AR antagonism in MDSCs may have directly affected glycolysis.

Myeloid cell metabolism supports myeloid cell function (13). As AR antagonism induced glycolysis and reduced basal mitochondrial respiration (**Fig. 4**), we hypothesized that one of these metabolic pathways was responsible for supporting the increased tumor-promoting ability of enzalutamide-treated myeloid cells (**Fig. 2**). To investigate whether increases in glycolysis were reflective of alterations in glucose uptake, glucose uptake and expression of GLUT1, the major transporter of glucose, were measured. Uptake of glucose was increased in enzalutamide-treated and MARKO BMDMs, and GLUT1 mRNA was induced with enzalutamide in BMDMs, suggesting that AR regulation of glycolysis was due, in part, to regulation of glucose uptake

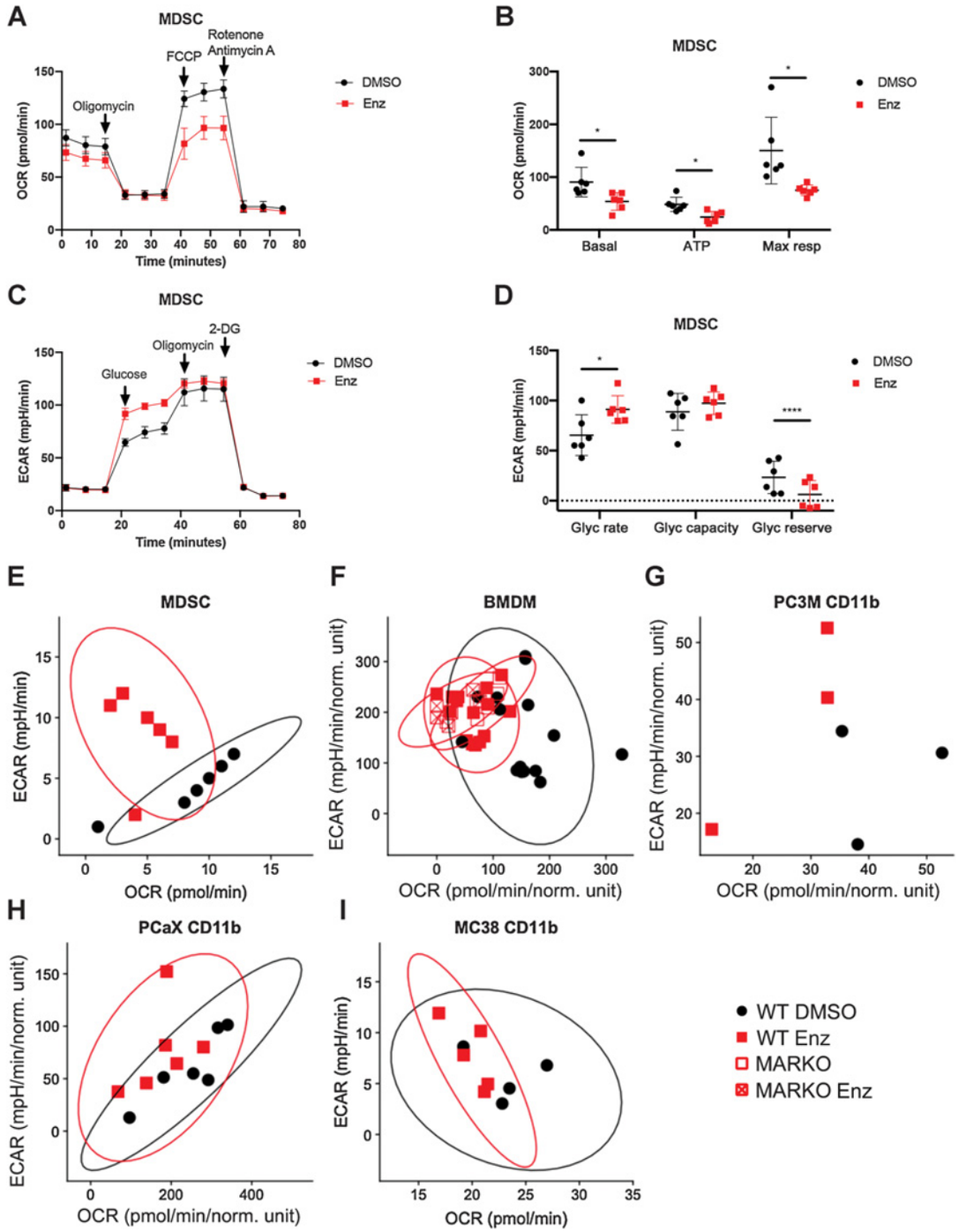

Figure 4.

Enzalutamide increased glycolysis and reduced mitochondrial respiration in myeloid cells. **A–D,** MDSCs were generated in DMSO or enzalutamide conditions and were assessed by Seahorse MitoStressTest (**A** and **B**) and GlycoStressTest (**C** and **D**). Graph indicates mean and SD for mitochondrial respiration test (**A**) and its calculated parameters (**B**). Graph indicates mean and SD for glycolytic test (**C**) and its calculated parameters (**D**). Metabolic profile plots depict glycolytic rate and basal mitochondrial respiration values from WT MDSCs generated *in vitro* in the presence of DMSO or enzalutamide (**E**), *in vitro* DMSO- or enzalutamide-treated WT and MARKO BMDMs (**F**), tumor-associated CD11b$^+$ cells from PCaX (**G**), and tumor-associated CD11b$^+$ cells from PC3M (**H**) for 24 hours. **I,** Plot depicts metabolic profile plot from CD11b$^+$ cells sorted from MC-38 tumor–bearing C57BL/6 males that were treated daily with saline or 20 mg/kg enzalutamide *in vivo* through oral gavage. Plots were made from pooled data from one to three experiments of three biological replicates per group. Ellipses from **E**, **F**, **H**, and **I** were estimated with ggplot2 in R. Black filled dots, DMSO treated; red filled squares, enzalutamide treated; red empty squares, MARKO; and red crossed squares, enzalutamide-treated MARKO myeloid cells. Plots indicate mean and SD. Statistical analyses were performed with paired tests (*, $P < 0.05$; ****, $P < 0.0001$). Enz, enzalutamide; Glyc, glycolytic; Max resp, maximal respiration.

(Supplementary Fig. S5A–S5C). However, targeting glycolysis with the glucose analogue 2-DG upon AR inhibition had a negative impact on MDSC cell number and metabolism (Supplementary Fig. S5D and S5E), further suggesting that the upregulation of glycolysis was compensating for the reduced mitochondrial respiration observed upon enzalutamide treatment.

These results suggested that the enzalutamide-induced increases in glycolysis may have been in response to direct effects of AR blockade on mitochondrial respiration. The reduction of mitochondrial respiration in myeloid cells following enzalutamide treatment may result from inhibition of starting material, that is, pyruvate or acetyl-CoA, or a decrease in mitochondrial mass or function, as measured by superoxide production (31). Enzalutamide treatment did not alter the mitochondrial labeling, superoxide production, or FAO needed for acetyl-CoA production (Supplementary Fig. S6A–S6E).

Enzalutamide-mediated decrease in mitochondrial respiration could have also been related to changes in proteins involved in mitochondrial coordination of the citric acid cycle (TCA) cycle and oxidative phosphorylation. Mitochondrial pyruvate carrier 2 (MPC-2) is a member of the MPC complex and a transcriptional target of AR in prostate cancer cells (32). MPC imports pyruvate formed by the glycolytic pathway into the mitochondria for TCA metabolism (33). MPC-2 was downregulated in BMDMs upon enzalutamide treatment in a dose-dependent manner (**Fig. 5H**). Inhibition of MPC with the inhibitor, UK-5509 (MPCi), lowered mitochondrial respiration in both BMDMs and MDSCs (Supplementary Fig. S6F and S6G). Therefore, to test whether inhibition of mitochondrial respiration increased the tumor-promoting ability of myeloid cells treated with enzalutamide, MDSCs were generated in the presence of DMSO or MPCi, mixed with MC-38 cells and, injected in C57BL/6 male mice. Inhibition of MPC in MDSCs resulted in accelerated MC-38 tumor growth (**Fig. 5I**), indicating that blocking mitochondrial respiration phenocopies myeloid AR blockade and enhances myeloid tumor–promoting activity.

Myeloid AR antagonism accelerated prostate tumor growth

Prostate cancer progression to CRPC involves various mechanisms of treatment resistance, and results in decreased patient survival (1). To determine whether AR deletion in myeloid cells was a mechanism implicated in CRPC, WT and MARKO C57BL/6 male mice were inoculated with TRAMP C2 prostate tumor cells, which were AR^+ (Supplementary Fig. S1A), and tumor growth was analyzed over time. Mice lacking AR expression in myeloid cells displayed faster tumor growth when compared with mice with intact AR signaling in myeloid cells (**Fig. 6A** and **B**). Similar, to myeloid–MC-38 mixture tumors (Supplementary Fig. S3C), MARKO mice did not alter tumor leukocyte infiltration when compared with WT mice (**Fig. 6C**), confirming that myeloid cell function, and not infiltration, was linked to accelerated tumor progression (**Fig. 6D**).

Discussion

Here, we demonstrated that enzalutamide, a commonly used hormone therapy that targets AR^+ tumor cells, directly impacted AR^+ myeloid cell function and metabolism (summarized in **Fig. 6D**). We showed that blocking myeloid AR enhanced myeloid cell tumor–promoting capacity, increased MDSC immunosuppression of T-cell proliferation, and increased tumor progression. We further described MPC-2– and AMPK-dependent changes in metabolism that promoted glycolysis over oxidative phosphorylation and were associated with an enhanced tumor-promoting phenotype.

AR blockade therapy impacts the tumor microenvironment indirectly and directly. In this study, AR antagonism affected myeloid cell function and metabolism similarly when genetic and pharmacologic approaches were used, suggesting that enzalutamide modulated myeloid cell phenotype through direct inhibition of AR. TAMs display a predominantly M2-like phenotype (34). Genetic deletion of AR in macrophages was associated with quicker cutaneous wound-healing responses (3), which is a characteristic of M2 macrophage function. However, AR deletion impairs M2 polarization in asthma (35). These results suggested that the effect of AR signaling in macrophages is context dependent, which may explain the contradictory findings concerning macrophage AR function in prostate tumorigenesis. Inhibition of macrophage AR delays prostate tumor development (4); however, prostate tumor progression and metastasis are enhanced in mice with AR-deficient macrophages (MARKO mice; ref. 11). Our findings concur with this study, as AR antagonism of myeloid cells enhanced their immunosuppressive function and enhanced myeloid tumor–promoting capacity and supported tumor progression. One potential explanation for the discrepancy in the effects of AR antagonism is that the frequencies of and functional interactions between tumor, stromal, and immune cells change over the course of tumorigenesis; therefore, the differential effects of inhibition of AR in macrophages on prostate tumor progression might be a consequence of this altered dynamics. Also, the extent to which myeloid AR antagonism affects tumor progression may depend on the aggressiveness of the tumor. In our study and in Izumi and colleagues' study (11), inhibition of myeloid AR enhanced tumor progression in tumor models that either grew rapidly or had already been established, respectively. Studies comparing slowly and aggressively progressing tumors could potentially clarify this question.

AR antagonism of prostate tumor cell lines and prostate tumor–bearing mice enhances macrophage migration and infiltration (12, 36). *In vivo* enzalutamide treatment results in secretion of prostate tumor–derived factors that induce macrophage polarization toward a tumor-promoting phenotype associated with treatment failure (12). AR antagonism in a murine prostate tumor model mediates immunosuppression by direct inhibition of T-cell activation (23). Our work built on these findings, showing that enzalutamide treatment enhanced myeloid cell immunosuppressive function. The combined evidence suggests that prostate cancer treatment with antiandrogens may ultimately contribute to tumor progression by increasing myeloid cell infiltration and by promoting immunosuppression.

Enzalutamide can have AR-independent effects such as the ability to inhibit GABA receptors in the brain (37). We observed divergence between pharmacologic and genetic approaches of AR blockade in the alteration of MDSC RNA expression, where enzalutamide treatment, but not AR knockout, induced VEGF and Arg1 mRNA and PD-L1 protein expression in MDSCs. These results implicated either a potential divergence in timing and penetrance of AR genetic knockout versus pharmacologic inhibition or, less likely, other unknown AR-independent mechanisms. Nonetheless, we demonstrated an AR-dependent enzalutamide modulation of myeloid cell function and metabolism. However, the specific signaling pathways involved in AR modulation of myeloid cell phenotype remains to be characterized.

Myeloid cell phenotype is tightly regulated by environmental cues and depends on metabolic changes that support effector functions (13). TAMs and MDSCs have high glycolytic rates that support tumor-promoting capacity and immunosuppression, respectively (14–17). We observed that enzalutamide treatment directly inhibited mitochondrial respiration and promoted glycolysis in myeloid cells; it is

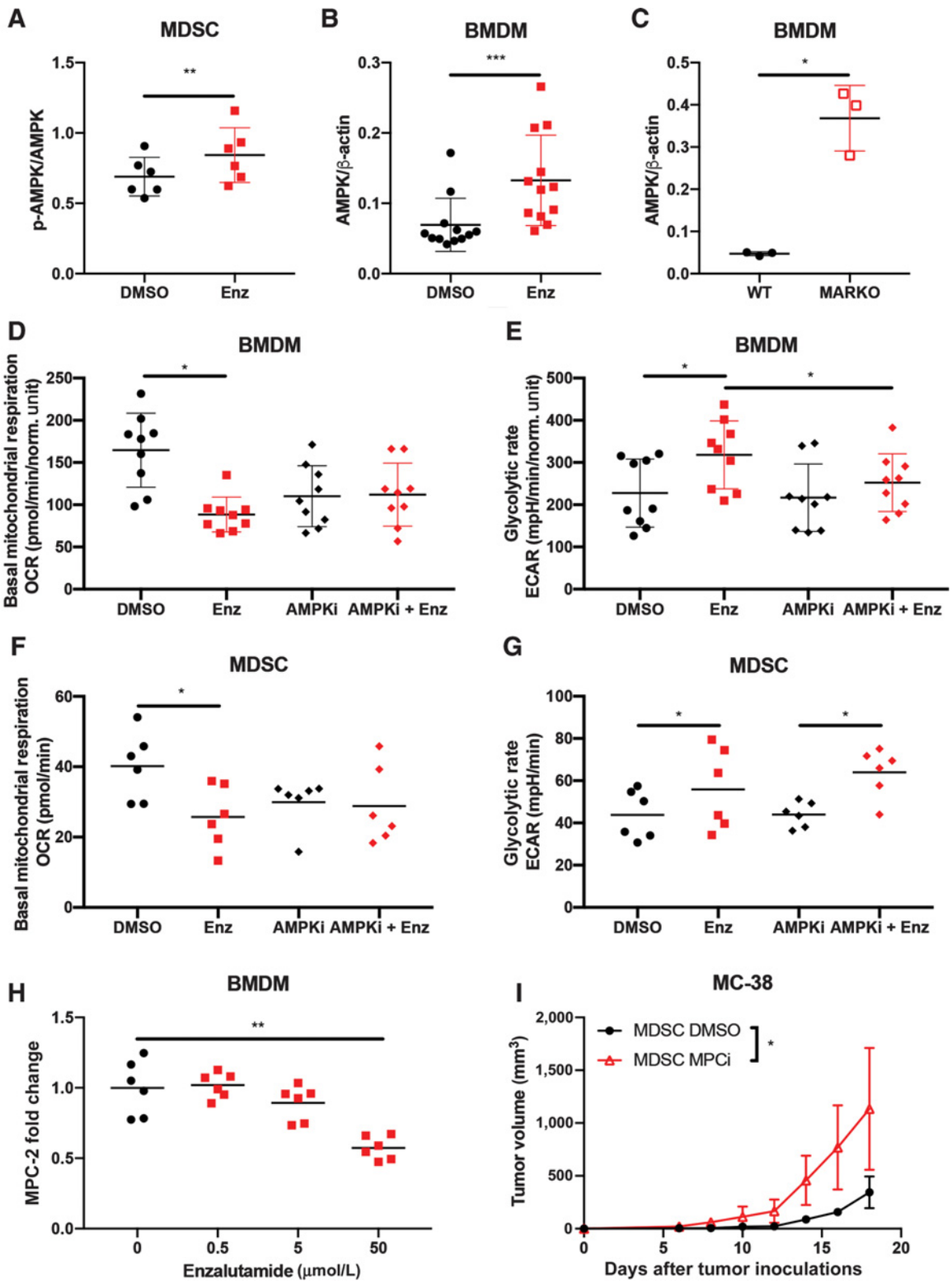

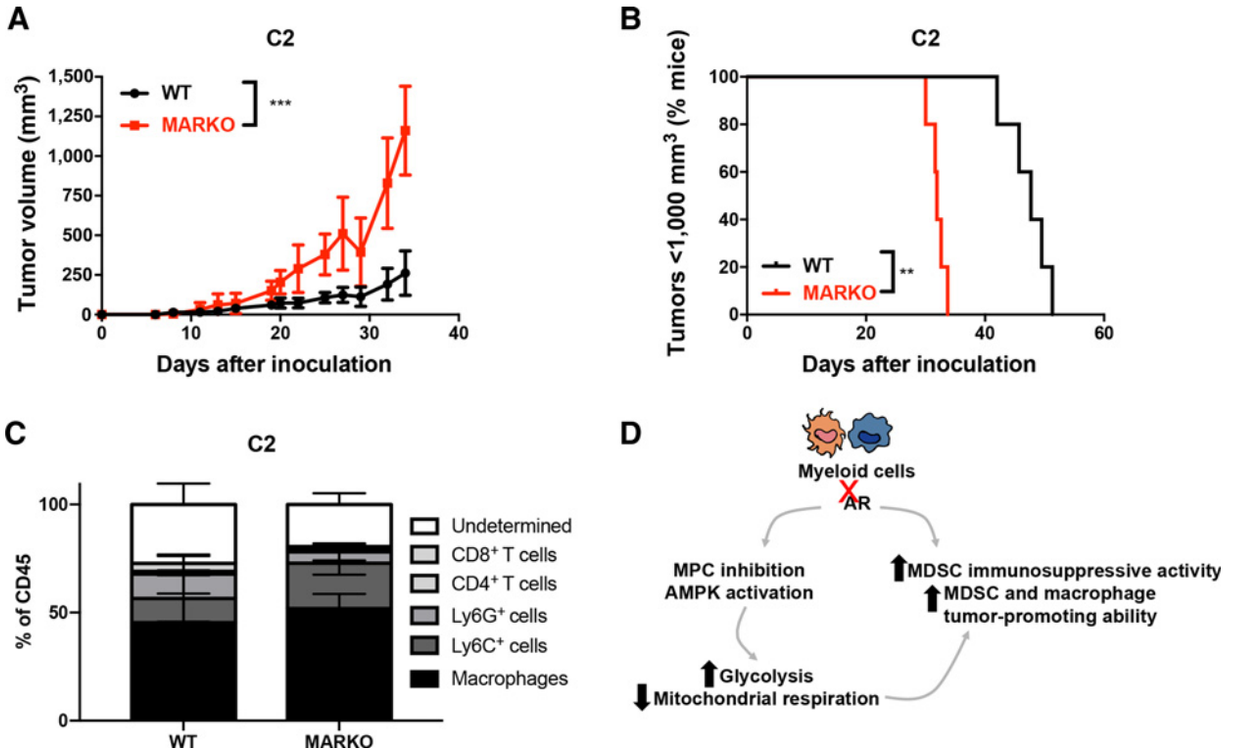

Figure 6.

Genetic deletion of AR in myeloid cells increased prostate tumor growth and progression. **A–C,** Tramp C2 prostate tumor cells were inoculated in WT and MARKO C56BL/6 male mice and followed for tumor growth. At the endpoint, tumors were assessed for leukocyte infiltration by flow cytometry. Graphs depict mean and SD of tumor growth over time (**A**), percentage of mice whose prostate cancer progressed (**B**), and C2 tumor leukocyte infiltration (**C**). **D,** Our proposed model, indicating that enzalutamide treatment of myeloid cells induces functional and metabolic changes, resulting in enhanced tumor progression. Black tumor growth curves denote WT mice, and red empty squares MARKO mice. Statistical analyses were done using two-way ANOVA and log-rank test (**, $P < 0.01$; ***, $P < 0.001$).

possible that this metabolic shift facilitated the tumor-promoting capacity of myeloid cells. Reduction of mitochondrial respiration with MPC inhibition phenocopied the enhanced tumor-promoting ability of MDSCs treated with enzalutamide, suggesting a metabolic mechanism by which AR antagonism in myeloid cells enhanced tumor progression. However, a causal link between metabolic changes induced by enzalutamide and the enhanced tumor-supporting capacity of myeloid cells needs to be established.

Two metabolic pathways were affected by AR inhibition of myeloid cells in our study, oxidative phosphorylation and glycolysis. AR antagonism reduced oxidative phosphorylation through the inhibition of the AR target MPC-2, thus potentially limiting pyruvate entry into the mitochondria. The increase in glycolysis following AR antagonism was likely an adaptation to the reduction in mitochondrial respiration and was needed to maintain cellular ATP, as inhibition of glycolysis significantly reduced MDSC cell number and metabolism. This hypothesis is in agreement with work in prostate cells where MPC-2 associates with subsequent induction of AMPK pathway and glycolysis (32). The role of AR in AMPK-mediated metabolism appears to be different between myeloid and prostate cancer cells. AR stimulation of prostate cancer cells, rather than inhibition, leads to induction of AMPK signaling to enhance glycolysis (18). Here, we identified that

Figure 5.

Enzalutamide-induced metabolic changes were mediated by AMPK in macrophages. **A,** MDSCs were generated in the presence of DMSO or enzalutamide and quantified for protein expression by Western blot analysis. Graph indicates p-AMPK/AMPK ratio. **B** and **C,** WT or MARKO BMDMs were treated with DMSO or enzalutamide for 24 hours, and protein expression was assessed by Western blotting. Plots indicate AMPK expression normalized to β-actin for DMSO- and enzalutamide-treated BMDMs (**B**) and WT and MARKO BMDMs (**C**). BMDMs were treated with DMSO or enzalutamide in the presence or absence of the AMPK inhibitor (AMPKi) dorsomorphin for 24 hours and were assessed by Seahorse MitoStressTest (**D**) and GlycoStressTest (**E**). Graphs show basal mitochondrial respiration (**D**) and indicate glycolytic rate (**E**) for BMDMs. MDSCs generated in the presence of DMSO or enzalutamide were treated with AMPKi for the last 24 hours of MDSC generation, and cells were assessed by Seahorse MitoStressTest (**F**) and GlycoStressTest (**G**). Graphs show basal mitochondrial respiration (**F**) and indicate glycolytic rate (**G**) for MDSCs. **H,** BMDMs were generated and treated with increasing doses of enzalutamide, and RNA expression was assessed by qRT-PCR. Graph depicts MPC-2 fold change in expression relative to 0 μmol/L enzalutamide. **I,** MDSCs generated *in vitro* in the presence of DMSO or the MPCi UK-5509 were mixed with MC-38 tumor cells in a 2:1 myeloid:tumor cell ratio and implanted subcutaneously on the shoulder of C57BL/6 male mice. Graph depicts tumor growth curves. Plots indicate mean, and, where noted, error bars indicate SD from pooled data of two to three experiments of three to five biological replicates per group. Black dots, DMSO treated; red squares, enzalutamide treated; black diamonds, AMPKi treated; red diamonds, enzalutamide and AMPKi treated; and red empty triangles, MPCi-treated myeloid cells. Statistical analyses were performed with nonparametric one-way ANOVA and paired tests with corrections when necessary (*, $P < 0.05$; **, $P < 0.01$; ***, $P < 0.001$). Enz, enzalutamide.

AR antagonism increased glycolytic and decreased oxidative phosphorylation metabolism through AMPK in macrophages. This divergent effect of AR activation/inhibition on AMPK-mediated downstream metabolic effects may be potentially explained by an AMPK–AR negative feedback loop (38); AR induces AMPK activation, which in turn inhibits AR transcriptional activity. By blocking AR in macrophages, this feedback loop could be lost and may potentially lead to increased AMPK activation, which in turn mediated the metabolic changes observed.

Whereas the effects of AR pharmacologic inhibition on metabolism were dependent on AMPK signaling in macrophages, enzalutamide only affected mitochondrial respiration through AMPK in MDSCs. It is still possible that AMPK was involved in enzalutamide-mediated upregulation of the glycolytic pathway in MDSCs, as timing of AMPK inhibition was designed to avoid cell death, but may not have been enough to inhibit enzalutamide-induced early AMPK activation. Indeed, AMPK activation of monocytic MDSCs with metformin induces glycolysis and, in turn, glycolysis is important for MDSC immunosuppressive ability (17).

Hormone receptors cross-regulate each other; AR increases and decreases estrogen receptor (ER) activity (39). ERα can increase MDSC mobilization and suppressive activity in a breast tumor model (40). Therefore, it is possible that the increased MDSC suppressive activity induced by AR blockade is due, in part, to the release of AR-mediated inhibition of ER signaling.

Our study highlighted the need to understand how sex hormone modulation therapies affect hormone receptor–positive nontumor cells within the tumor microenvironment. It is apparent from our studies and others that sex hormone antagonism affects multiple cell types within the tumor microenvironment. Tumor resistance to hormone blockade therapies may be associated with the varied responses coming from the complex tumor microenvironment. Here, we identified a mechanism of AR antagonism resistance that affected antitumor immunity directly through myeloid cells. Dissecting this complexity may indicate pathways that can be targeted to increase cancer patient survival. Alternatively, sex hormone receptor targeting can also be used as a strategy to boost antitumor immune responses. ER antagonism is standard of care in patients with ER^+, but not in ER^- breast tumor. However, MDSC accumulation and immunosuppressive functions are increased with estrogen stimulation, and targeting MDSC ERα reverses these effects in various ER-independent tumor models (40). This suggests that targeting ERs in ER^- tumors induces a beneficial immunologic rewiring toward enhanced antitumor immune responses. Alternatively, even though sex hormone receptor inhibition may have detrimental immunomodulatory effects, as shown here and by Pu and colleagues (23), it may be possible to ameliorate these effects by combination with novel therapies that release this immunomodulatory constraint. One avenue to achieve this is to stimulate antitumor immune responses by metabolic rewiring. Macrophage phagocytic function is enhanced by CpG-mediated induction of FAO, resulting in more efficient cancer cell clearance and delayed tumor progression (41). Future studies will be needed to investigate whether reversal of enzalutamide-induced metabolic changes in myeloid cells can be targeted to enhance antitumor immunity.

In summary, our work demonstrated that AR signaling affects myeloid cell function and metabolism leading to enhanced tumor-promoting capability in both colon and prostate cancer models. These findings suggest that although AR blockade could inhibit prostate tumor growth, it also promoted tumor resistance by enhancing the immunosuppressive activity of myeloid cells.

Disclosure of Potential Conflicts of Interest

No potential conflicts of interest were disclosed.

Authors' Contributions

C.R. Consiglio: Conceptualization, investigation, methodology, writing–original draft, writing–review and editing. **O. Udartseva:** Investigation, writing–review and editing. **K.D. Ramsey:** Investigation. **C. Bush:** Investigation. **S.O. Gollnick:** Conceptualization, resources, supervision, funding acquisition, writing–original draft, project administration, writing–review and editing.

Acknowledgments

Research reported in this article was supported, in part, by the NCI of the NIH under award 5P01CA98156 (to S.O. Gollnick) and the Roswell Park Alliance Foundation. The study used shared resources supported by the Roswell Park Cancer Institute Cancer Center Support Grant (P30CA016056). C.R. Consiglio was supported by the Mark Diamond Research Fund from the Graduate Student Association at University at Buffalo and the Chateaubriand Fellowship. The authors acknowledge Roswell Park's Flow Cytometry core, Kieran O'Loughlin, and Dr. Subhamoy Dasgupta for the technical support and insightful discussions. C. Bush was supported by the U.S. Department of Defense under award PC131811.

The costs of publication of this article were defrayed in part by the payment of page charges. This article must therefore be hereby marked *advertisement* in accordance with 18 U.S.C. Section 1734 solely to indicate this fact.

Received May 20, 2019; revised October 2, 2019; accepted June 30, 2020; published first July 13, 2020.

References

1. Mitsiades N. A road map to comprehensive androgen receptor axis targeting for castration-resistant prostate cancer. Cancer Res 2013;73:4599–605.
2. Cuzick J, Howell A. A brief review of the breast cancer prevention trials. Eur J Cancer 2000;36:S51–3.
3. Lai JJ, Lai KP, Chuang KH, Chang P, Yu IC, Lin WJ, et al. Monocyte/macrophage androgen receptor suppresses cutaneous wound healing in mice by enhancing local TNF-alpha expression. J Clin Invest 2009;119:3739–51.
4. Fang LY, Izumi K, Lai KP, Liang L, Li L, Miyamoto H, et al. Infiltrating macrophages promote prostate tumorigenesis via modulating androgen receptor-mediated CCL4-STAT3 signaling. Cancer Res 2013; 73:5633–46.
5. Leach DA, Need EF, Toivanen R, Trotta AP, Palethorpe HM, Tamblyn DJ, et al. Stromal androgen receptor regulates the composition of the microenvironment to influence prostate cancer outcome. Oncotarget 2015;6: 16135–50.
6. Walecki M, Eisel F, Klug J, Baal N, Paradowska-Dogan A, Wahle E, et al. Androgen receptor modulates Foxp3 expression in CD4+CD25+Foxp3+ regulatory T-cells. Mol Biol Cell 2015;26:2845–57.
7. Calcinotto A, Spataro C, Zagato E, Mitri DD, Gil V, Crespo M, et al. IL-23 secreted by myeloid cells drives castration-resistant prostate cancer. Nature 2018;559:363–9.
8. Qian B-Z, Pollard JW. Macrophage diversity enhances tumor progression and metastasis. Cell 2010;141:39–51.
9. Lissbrant IF, Stattin P, Wikstrom P, Damber JE, Egevad L, Bergh A. Tumor associated macrophages in human prostate cancer: relation to clinicopathological variables and survival. Int J Oncol 2000;17:445–51.
10. Zhao X, Qu J, Sun Y, Wang J, Liu X, Wang F, et al. Prognostic significance of tumor-associated macrophages in breast cancer: a meta-analysis of the literature. Oncotarget 2017;8:30576–86.
11. Izumi K, Fang LY, Mizokami A, Namiki M, Li L, Lin WJ, et al. Targeting the androgen receptor with siRNA promotes prostate cancer metastasis through enhanced macrophage recruitment via CCL2/CCR2-induced STAT3 activation. EMBO Mol Med 2013;5:1383–401.
12. Escamilla J, Schokrpur S, Liu C, Priceman SJ, Moughon D, Jiang Z, et al. CSF1 receptor targeting in prostate cancer reverses macrophage-mediated resistance to androgen blockade therapy. Cancer Res 2015;75:950–62.

13. O'Neill LA, Pearce EJ. Immunometabolism governs dendritic cell and macrophage function. J Exp Med 2016;213:15–23.
14. Penny HL, Sieow JL, Adriani G, Yeap WH, Ee PSC, Luis BS, et al. Warburg metabolism in tumor-conditioned macrophages promotes metastasis in human pancreatic ductal adenocarcinoma. Oncoimmunology 2016;5:e1191731.
15. Hossain F, Al-Khami AA, Wyczechowska D, Hernandez C, Zheng L, Reiss K, et al. Inhibition of fatty acid oxidation modulates immunosuppressive functions of myeloid-derived suppressor cells and enhances cancer therapies. Cancer Immunol Res 2015;3:1236–47.
16. Liu D, Chang C, Lu N, Wang X, Lu Q, Ren X, et al. Comprehensive proteomics analysis reveals metabolic reprogramming of tumor-associated macrophages stimulated by the tumor microenvironment. J Proteome Res 2017;16:288–97.
17. Wu T, Zhao Y, Wang H, Li Y, Shao L, Wang R, et al. mTOR masters monocytic myeloid-derived suppressor cells in mice with allografts or tumors. Sci Rep 2016; 6:20250.
18. Massie CE, Lynch A, Ramos-Montoya A, Boren J, Stark R, Fazli L, et al. The androgen receptor fuels prostate cancer by regulating central metabolism and biosynthesis. EMBO J 2011;30:2719–33.
19. Kumar MP, Du J, Lagoudas G, Jiao Y, Sawyer A, Drummond DC, et al. Analysis of single-cell RNA-seq identifies cell-cell communication associated with tumor characteristics. Cell Rep 2018;25:1458–68.
20. Foster BA, Gingrich JR, Kwon ED, Madias C, Greenberg NM. Characterization of prostatic epithelial cell lines derived from transgenic adenocarcinoma of the mouse prostate (TRAMP) model. Cancer Res 1997;57:3325–30.
21. De Gendt K, Swinnen JV, Saunders PTK, Schoonjans L, Dewerchin M, Devos A, et al. A Sertoli cell-selective knockout of the androgen receptor causes spermatogenic arrest in meiosis. Proc Natl Acad Sci U S A 2004;101:1327–32.
22. Marigo I, Bosio E, Solito S, Mesa C, Fernandez A, Dolcetti L, et al. Tumor-induced tolerance and immune suppression depend on the C/EBPbeta transcription factor. Immunity 2010;32:790–802.
23. Pu Y, Xu M, Liang Y, Yang K, Guo Y, Yang X, et al. Androgen receptor antagonists compromise T cell response against prostate cancer leading to early tumor relapse. Sci Transl Med 2016;8:333ra47.
24. Lin N, Simon MC. Hypoxia-inducible factors: key regulators of myeloid cells during inflammation. J Clin Invest 2016;126:3661–71.
25. Byles V, Covarrubias AJ, Ben-Sahra I, Lamming DW, Sabatini DM, Manning BD, et al. The TSC-mTOR pathway regulates macrophage polarization. Nat Commun 2013;4:2834.
26. Everts B, Amiel E, Huang SCC, Smith AM, Chang CH, Lam WY, et al. TLR-driven early glycolytic reprogramming via the kinases TBK1-IKKvarepsilon supports the anabolic demands of dendritic cell activation. Nat Immunol 2014;15:323–32.
27. Achyut BR, Angara K, Jain M, Borin TF, Rashid MH, Iskander ASM, et al. Canonical NFκB signaling in myeloid cells is required for the glioblastoma growth. Sci Rep 2017;7:13754.
28. Cui Y, Nadiminty N, Liu C, Lou W, Schwartz CT, Gao AC. Upregulation of glucose metabolism by NF-κB2/p52 mediates enzalutamide resistance in castration-resistant prostate cancer cells. Endocr Relat Cancer 2014;21:435–42.
29. Salminen A, Kauppinen A, Kaarniranta K. AMPK activation inhibits the functions of myeloid-derived suppressor cells (MDSC): impact on cancer and aging. J Mol Med 2019;97:1049–64.
30. Zhu YP, Brown JR, Sag D, Zhang L, Suttles J. Adenosine 5'-monophosphate-activated protein kinase regulates IL-10-mediated anti-inflammatory signaling pathways in macrophages. J Immunol 2015;194:584–94.
31. Huttemann M, Lee I, Samavati L, Yu H, Doan JW. Regulation of mitochondrial oxidative phosphorylation through cell signaling. Biochim Biophys Acta 2007; 1773:1701–20.
32. Bader DA, Hartig SM, Putluri V, Foley C, Hamilton MP, Smith EA, et al. Mitochondrial pyruvate import is a metabolic vulnerability in androgen receptor-driven prostate cancer. Nature Metabolism 2019;1:70–85.
33. Bricker DK, Taylor EB, Schell JC, Orsak T, Boutron A, Chen YC, et al. A mitochondrial pyruvate carrier required for pyruvate uptake in yeast, Drosophila, and humans. Science 2012;337:96–100.
34. Grivennikov SI, Greten FR, Karin M. Immunity, inflammation, and cancer. Cell 2010;140:883–99.
35. Becerra-Diaz M, Strickland AB, Keselman A, Heller NM. Androgen and androgen receptor as enhancers of M2 macrophage polarization in allergic lung inflammation. J Immunol 2018;201:2923–33.
36. Lin TH, Izumi K, Lee SO, Lin WJ, Yeh S, Chang C. Anti-androgen receptor ASC-J9 versus anti-androgens MDV3100 (enzalutamide) or Casodex (bicalutamide) leads to opposite effects on prostate cancer metastasis via differential modulation of macrophage infiltration and STAT3-CCL2 signaling. Cell Death Dis 2013;4: e764.
37. Foster WR, Car BD, Shi H, Levesque PC, Obermeier MT, Gan J, et al. Drug safety is a barrier to the discovery and development of new androgen receptor antagonists. Prostate 2011;71:480–8.
38. Jurmeister S, Ramos-Montoya A, Neal DE, Fryer LGD. Transcriptomic analysis reveals inhibition of androgen receptor activity by AMPK in prostate cancer cells. Oncotarget 2014;5:3785–99.
39. Majumder A, Singh M, Tyagi SC. Post-menopausal breast cancer: from estrogen to androgen receptor. Oncotarget 2017;8:102739–58.
40. Svoronos N, Perales-Puchalt A, Allegrezza MJ, Rutkowski MR, Payne KK, Tesone AJ, et al. Tumor cell-independent estrogen signaling drives disease progression through mobilization of myeloid-derived suppressor cells. Cancer Discov 2017;7:72–85.
41. Liu M, O'Connor RS, Trefely S, Graham K, Snyder NW, Beatty GL. Metabolic rewiring of macrophages by CpG potentiates clearance of cancer cells and overcomes tumor-expressed CD47-mediated 'don't-eat-me' signal. Nat Immunol 2019;20:265–75.